

On acoustic cavitation of slightly subcritical bubbles

Anthony Harkin[†] Ali Nadim[‡] Tasso J. Kaper[†]

[†]Department of Mathematics, Boston University, Boston, MA 02215

[‡]Department of Aerospace and Mechanical Engineering, Boston University, Boston, MA 02215

July 24, 1998

Abstract

The classical Blake threshold indicates the onset of quasistatic evolution leading to cavitation for gas bubbles in liquids. When the mean pressure in the liquid is reduced to a value below the vapor pressure, the Blake analysis identifies a critical radius which separates quasistatically stable bubbles from those which would cavitate. In this work, we analyze the cavitation threshold for radially symmetric bubbles whose radii are slightly less than the Blake critical radius, in the presence of time-periodic acoustic pressure fields. A distinguished limit equation is derived that predicts the threshold for cavitation for a wide range of liquid viscosities and forcing frequencies. This equation also yields frequency-amplitude response curves. Moreover, for fixed liquid viscosity, our study identifies the frequency that yields the minimal forcing amplitude sufficient to initiate cavitation. Numerical simulations of the full Rayleigh-Plesset equation confirm the accuracy of these predictions. Finally, the implications of these findings for acoustic pressure fields that consist of two frequencies will be discussed.

PACS Numbers: Primary 43.25.Yw, Secondary 43.25.Ts, 47.52.+j, 43.25.Rq

Keywords: acoustic cavitation, nonlinear oscillations of gas bubbles, dynamic cavitation threshold, periodic pressure fields, quasiperiodic pressure fields, period-doubling.

I Introduction

The Blake threshold pressure is the standard measure of static acoustic cavitation [2, 1]. Bubbles forced at pressures exceeding the Blake threshold grow quasistatically without bound. This criterion is especially important for gas bubbles in liquids when surface tension is the dominant effect, such as submicron air bubbles in water, where the natural oscillation frequencies are high.

In contrast, when the acoustic pressure fields are not quasistatic, bubbles generally evolve in highly nonlinear fashions [21, 9, 16, 17]. To begin with, the intrinsic oscillations of spherically symmetric bubbles in inviscid incompressible liquids are nonlinear [16]. The phase portrait of the Rayleigh-Plesset equation [26, 25, 4], consists of a large region of bounded, stable states centered about the stable equilibrium radius. The natural oscillation frequencies of these states depend on the initial bubble radius and its radial momentum, and this family of states limits on a state of infinite period, namely a homoclinic orbit in the phase space, which acts as a boundary outside of which lie initial conditions corresponding to unstable bubbles. Time-dependent acoustic pressure fields then interact nonlinearly with both the periodic orbits and the homoclinic orbit. In particular, they can act to break the homoclinic orbit, permitting initially stable bubbles to leave the stable region and grow without bound. These interactions have been studied from many points of view: experimentally, numerically, and analytically via perturbation theory and techniques from dynamical systems.

In [26], the transition between regular and chaotic oscillations, as well as the onset of rapid radial growth, is studied for spherical gas bubbles in time-dependent pressure fields. There, Melnikov theory is applied to the periodically- and quasiperiodically-forced Rayleigh-Plesset equation for bubbles containing an isothermal gas. One of the principal findings is that, when the acoustic pressure field is quasiperiodic in time with two or more frequencies, the transition to chaos and the threshold for rapid growth occur at lower amplitudes of the acoustic pressure field than in the case of single-frequency forcing. Their work was motivated in turn by that in [13], where Melnikov theory was used to study the time-dependent shape changes of gas bubbles in time-periodic axisymmetric strain fields.

The work in [25] identifies a rich bifurcation superstructure for radial oscillations for bubbles in time-periodic acoustic pressure fields. Techniques from perturbation theory and dynamical systems are used to analyze resonant subharmonics, period-doubling bifurcation sequences, the disappearance of strange attractors, and transient chaos in the Rayleigh-Plesset equation with small-amplitude liquid viscosity and isentropic gas. The analysis in [25] complements the experiments of [8] and the experiments and numerical simulations of [14, 15, 20]. Analyzing subharmonics, these works quantify the impact of increasing the amplitude of the acoustic pressure field on the frequency-response curves.

Other works examining the threshold for acoustic cavitation in time-dependent pressure fields have focused on the case of a step change in pressure. In [4], the response of a gas bubble to such a step change in pressure is analyzed by numerical and Melnikov perturbation techniques to find a correlation between the cavitation pressure and the viscosity of the liquid. One of the principal findings is that the cavitation pressure scales as the one-fifth power of the liquid viscosity. A general method to compute the critical conditions for an instantaneous pressure step is also given in [7]. The results extend numerical simulations of [19] and

experimental findings of [24], and apply for any value of the polytropic gas exponent.

The goal of the present article is to apply similar perturbation methods and techniques from the theory of nonlinear dynamical systems to refine the Blake cavitation threshold for isothermal bubbles whose radii are slightly smaller than the critical Blake radius and whose motions are not quasistatic. Specifically, we suppose these bubbles are subjected to time-periodic acoustic pressure fields and, by reducing the Rayleigh-Plesset equations to a simpler distinguished limit equation, we obtain the dynamic cavitation threshold for these subcritical bubbles.

The paper is organized as follows. In the remainder of this section, the standard Blake cavitation threshold is briefly reviewed. This also allows us to identify the critical radius which separates stable and unstable bubbles that are in equilibrium. In section II, the distinguished limit (or normal form) equation of motion for subcritical bubbles (*i.e.*, those whose radii is slightly smaller than the critical value) is obtained from the Rayleigh-Plesset equation. This necessitates identifying the natural timescale of oscillation of such subcritical bubbles which happens to depend upon how close they are to the critical size. We begin section III by defining a simple criterion for determining when cavitation has occurred. We then analyze the normal form equation and determine the cavitation threshold for a specific value of the acoustic forcing frequency (at which the corresponding linear undamped system would resonate). This pressure threshold is then compared to numerical simulations of the full Rayleigh-Plesset equation and the good agreement found between the two is demonstrated. The self-consistency of the distinguished limit equation is further discussed in that section. Section IV generalizes the results to include arbitrary acoustic forcing frequencies. Acoustic forcing frequencies which facilitate cavitation using the least forcing pressure are determined. An unusual dependence of the threshold pressure on forcing frequency is discovered and explained by analyzing the “slowly-varying” phase-plane of the dynamical system. At the end of section IV, our choice of a cavitation criterion is discussed in the setting of a Melnikov analysis. In section V we extend the cavitation results to the case of an oscillating subcritical bubble that is driven simultaneously at two different frequencies. We recap the paper in section VI by highlighting the main results and discussing their applicability. Lastly, we conclude the paper with an appendix which qualitatively discusses the relation of our results to some recent experimental findings.

I.1 Blake threshold pressure

To facilitate the development of subsequent sections we first briefly review the derivation of the Blake threshold [17]. At equilibrium, the pressure, p_B , inside a spherical bubble of radius R is related to the pressure, p_L , of the outside liquid through the normal stress balance across the surface:

$$p_B = p_L + \frac{2\sigma}{R}. \quad (1)$$

The pressure inside the bubble consists of gas pressure and vapor pressure, $p_B = p_g + p_v$, where the vapor pressure p_v is taken to be constant — p_v depends primarily on the temperature of the liquid — and the pressure of the gas is assumed to be given by the equation of state:

$$p_g = p_{g0} \left(\frac{R_0}{R} \right)^{3\gamma}, \quad (2)$$

with γ the polytropic index of the gas. For isothermal conditions $\gamma = 1$, whereas for adiabatic ones, γ is the ratio of constant-pressure to constant-volume heat capacities. At equilibrium, the bubble has radius R_0 , the gas has pressure p_{g0} and the static pressure of the liquid is taken to be p_0^∞ . Thus, the equilibrium pressure of the gas in the bubble is given by

$$p_{g0} = p_0^\infty - p_v + \frac{2\sigma}{R_0}.$$

Upon substituting this result into (2) we get the following expression for the pressure of the gas inside the bubble as a function of the bubble radius:

$$p_g = \left(p_0^\infty - p_v + \frac{2\sigma}{R_0} \right) \left(\frac{R_0}{R} \right)^{3\gamma}. \quad (3)$$

Upon combining equations (1) and (3), we find

$$p_L = \left(p_0^\infty - p_v + \frac{2\sigma}{R_0} \right) \left(\frac{R_0}{R} \right)^{3\gamma} + p_v - \frac{2\sigma}{R}. \quad (4)$$

Equation (4) governs the change in the radius of a bubble in response to quasistatic changes in the liquid pressure p_L . More precisely, by “quasistatic” we mean that the liquid pressure changes slowly and uniformly with inertial and viscous effects remaining negligible during expansion or contraction of the bubble. For very small (sub-micron) bubbles, surface tension is the dominant effect. Furthermore, typical acoustic forcing frequencies are much smaller than the resonance frequencies of such tiny bubbles. In this case, the pressure in the liquid changes very slowly and uniformly compared to the natural timescale of the bubble.

For very small bubbles, the Peclet number for heat transfer within the bubble — defined as $R_0^2\omega/\alpha$, with ω the bubble natural frequency (see subsection II.1) and α the thermal diffusivity of the gas — is small, and due to the rapidity of thermal conduction over such small length scales, the bubble may be regarded as isothermal. We therefore let $\gamma = 1$ for an isothermal bubble and define

$$\tilde{G} = \left(p_0^\infty - p_v + \frac{2\sigma}{R_0} \right) R_0^3.$$

Then equation (4) becomes

$$p_L = p_v + \frac{\tilde{G}}{R^3} - \frac{2\sigma}{R}. \quad (5)$$

The right-hand side of this equation is plotted in figure 1 (solid curve), which shows a minimum value at a critical radius labeled R_{crit} .

Obviously, if the liquid pressure is lowered to a value below the corresponding critical pressure $p_{L_{\text{crit}}}$, no equilibrium radius exists. For values of p_L which are above the critical value but below the vapor pressure p_v , equation (5) yields two possible solutions for the radius R . Bubbles whose radii are less than the Blake radius, R_{crit} , are stable to small disturbances, whereas bubbles with $R > R_{\text{crit}}$ are unstable to small disturbances.

The Blake radius itself can be obtained by finding the minimum of the right-hand side of (5) for $R > 0$. This yields the critical Blake radius

$$R_{\text{crit}} = \left(\frac{3\tilde{G}}{2\sigma} \right)^{1/2}, \quad (6)$$

at which the corresponding critical liquid pressure is

$$p_{L_{\text{crit}}} = p_v - \left(\frac{32\sigma^3}{27\tilde{G}} \right)^{1/2}. \quad (7)$$

By combining the last two equations, it is also possible to express the Blake radius in the form:

$$R_{\text{crit}} = \frac{4\sigma}{3(p_v - p_{L_{\text{crit}}})},$$

relating the critical bubble radius to the critical pressure in the liquid. Bubbles whose radii are smaller than R_{crit} are quasistatically stable, while bigger ones are unstable.

To obtain the standard Blake pressure we assume that p_v can be ignored and recall that surface tension dominates in the quasistatic regime which amounts to $p_0^\infty \ll 2\sigma/R_0$. Under these approximations, $\tilde{G} \approx 2\sigma R_0^2$ and the Blake threshold pressure is conventionally defined as

$$\begin{aligned} p_{\text{Blake}} &\equiv p_0^\infty - p_{L_{\text{crit}}} \\ &\approx p_0^\infty + 0.77 \frac{\sigma}{R_0}. \end{aligned}$$

In the quasistatic regime where the Blake threshold is valid, p_{Blake} is the amplitude of the low-frequency acoustic pressure beyond which acoustic forcing at higher pressures is sure to cause cavitation. When the pressure changes felt by the bubble are no longer quasistatic, a more detailed analysis taking into consideration the bubble dynamics and acoustic forcing frequency must be performed to determine the cavitation threshold. This is the type of analysis we undertake in this contribution.

II The distinguished limit equation

II.1 Derivation

To make progress analytically, we focus our attention on “subcritical” bubbles whose radii are only slightly smaller than the Blake radius at a given liquid pressure below the vapor pressure. We thus define a small parameter $\epsilon > 0$ by

$$\epsilon = 2 \left[1 - \frac{R_0}{R_{\text{crit}}} \right], \quad (8)$$

which measures how close the equilibrium bubble radius R_0 is to the critical value R_{crit} . The value of the mean pressure in the liquid, corresponding to the equilibrium radius R_0 , can also be found from equation (5) to be

$$p_0^\infty - p_v = \frac{2\sigma}{3R_0} [(1 - \frac{\epsilon}{2})^{-2} - 3] = -\frac{4\sigma}{3R_0} [1 - \frac{1}{2}\epsilon - \frac{3}{8}\epsilon^2 + \mathcal{O}(\epsilon^3)]. \quad (9)$$

The liquid pressure p_0^∞ and the critical pressure $p_{L_{\text{crit}}}$ differ only by an $\mathcal{O}(\epsilon^2)$ amount.

It turns out that the characteristic time scale for the natural response of such subcritical bubbles also depends on the small parameter ϵ . This timescale for small amplitude oscillations of a spherical bubble is obtained by linearizing the isothermal, unforced Rayleigh-Plesset equation [21]

$$\rho \left[R \ddot{R} + \frac{3}{2} \dot{R}^2 \right] = \left(p_0^\infty - p_v + \frac{2\sigma}{R_0} \right) \left(\frac{R_0}{R} \right)^3 + p_v - \frac{2\sigma}{R} - p_0^\infty, \quad (10)$$

where the density of the liquid is given by ρ and viscosity has been neglected. Specifically, we substitute $R = R_0(1 + x)$ into (10) and keep terms linear in x to get:

$$\ddot{x} + \left[\frac{4\sigma}{\rho R_0^3} + \frac{3(p_0^\infty - p_v)}{\rho R_0^2} \right] x = 0. \quad (11)$$

Solutions to (11), representing small amplitude oscillations about equilibrium, are therefore $x = x_0 \cos(\omega t + \phi)$ with the angular frequency given by

$$\omega = \left[\frac{4\sigma}{\rho R_0^3} + \frac{3(p_0^\infty - p_v)}{\rho R_0^2} \right]^{1/2}. \quad (12)$$

We now use ω to define a nondimensional time variable: $\tau = \omega t$. We are interested in analyzing stability for values of (R_0, p_0^∞) near $(R_{\text{crit}}, p_{L_{\text{crit}}})$. Hence, upon recalling (6), (7) and (8), we see that:

$$\tau = \left[\frac{2\sigma}{\rho R_0^3} \left(2 \left[1 - \frac{R_0}{R_{\text{crit}}} \right] \right) \right]^{1/2} t = \left[\frac{2\sigma\epsilon}{\rho R_0^3} \right]^{1/2} t.$$

We note that as ϵ tends to zero, the timescale for bubble oscillations (the reciprocal of the factor multiplying t in the last equation) increases as $\epsilon^{-1/2}$.

Having determined the proper scaling for the time variable for slightly subcritical bubbles, we can now find the distinguished limit (or normal form) equation for such bubbles in a time-periodic pressure field. We start with the isothermal, viscous Rayleigh-Plesset equation [21]:

$$\rho \left[R \ddot{R} + \frac{3}{2} \dot{R}^2 \right] + 4\mu \frac{\dot{R}}{R} = \left(p_0^\infty - p_v + \frac{2\sigma}{R_0} \right) \left(\frac{R_0}{R} \right)^3 + p_v - \frac{2\sigma}{R} - p_0^\infty + p_A \sin(\Omega t). \quad (13)$$

The amplitude and frequency of the applied acoustic forcing are given by p_A and Ω , respectively, and μ represents the viscosity of the fluid. Here, the far-field pressure in the liquid has been taken to be $p_0^\infty - p_A \sin(\Omega t)$, with p_0^∞ given by equation (9). Setting $R(t) = R_0(1 + \epsilon x(\tau))$, with ϵ the same small parameter introduced above, we obtain at order ϵ^2 (noting that all of the $\mathcal{O}(1)$ and $\mathcal{O}(\epsilon)$ terms cancel):

$$\ddot{x} + 2\zeta\dot{x} + x - x^2 = A \sin(\Omega^* \tau), \quad (14)$$

where

$$\zeta = \left(\frac{2\mu^2}{\epsilon\sigma\rho R_0} \right)^{1/2}, \quad A = \frac{p_A R_0}{2\sigma\epsilon^2}, \quad \Omega^* = \Omega \left(\frac{\rho R_0^3}{2\sigma\epsilon} \right)^{1/2}. \quad (15)$$

In equation (14), each overdot represents a derivative with respect to τ .

It is implicit in the above scaling that ζ , A , and Ω^* are nondimensional and $\mathcal{O}(1)$ with respect to ϵ . To see that this is reasonable, consider an air bubble in water with $\rho = 998 \text{ kg/m}^3$, $\mu = 0.001 \text{ kg/m}\cdot\text{s}$, $\sigma = 0.0725 \text{ N/m}$. If we specify $\epsilon = 0.1$ and take a modest equilibrium radius of $R_0 = 2 \times 10^{-6} \text{ m}$ then $\zeta = 0.38$. Our analysis of (14) in subsequent sections will concentrate primarily on values of ζ in the range $0 \leq \zeta \leq 0.4$. The parameters A and Ω^* are related to the forcing conditions, and their magnitudes can be made order unity by choosing appropriate forcing parameters p_A and Ω . As an example, if we again choose R_0 to equal 2 microns, then $\Omega^* = (2.35 \times 10^{-7} \text{ s})\Omega/\sqrt{\epsilon}$. Moreover, setting $\epsilon = 0.05$ gives $\Omega^* = (1.05 \times 10^{-6} \text{ s})\Omega$. Hence, the dimensionless parameter Ω^* is $\mathcal{O}(1)$ when Ω is in the megahertz range, and this is precisely the frequency range we are interested in exploring. Similarly, with R_0 and σ chosen as above, we find $A = (1.38 \times 10^{-5} \text{ m}\cdot\text{s}^2/\text{kg})p_A/\epsilon^2$ and thereby we see that if $\epsilon = 0.1$ then p_A can become on the order of 10^3 Pa . More data will be presented later, in figure 9, showing typical forcing pressures.

II.2 Interpretation

In the laboratory one can create a subcritical bubble by subjecting the liquid to a low-frequency transducer whose effect is to lower the ambient pressure below the vapor pressure. Then a second transducer of high

frequency (high relative to the slow transducer) will give rise to the forcing term on the right hand side of (14). The low-frequency transducer periodically increases and decreases the pressure in the liquid (and shrinks and expands the bubble, which follows this pressure field quasistatically). When the peak negative pressure is reached (and the bubble has expanded to its maximum size), we can imagine that state as the new equilibrium state, and at that point bring in the effects of the sound from the second transducer. This second field can then possibly make the bubble, which had already grown to some large size (but still smaller than the critical radius), become unstable. This would all happen very fast compared to the time scale of the original slow transducer, so the pressure field contributed by the original transducer remains near its most negative value throughout. The stability response of the bubble to the high frequency component of the pressure field is the subject of the rest of this work.

III Acoustic forcing thresholds ($\Omega^* = 1$)

The value of $\Omega^* = 1$ corresponds to the forcing frequency at which the linear and undamped counterpart of (14) would resonate. We therefore choose this value of the forcing frequency as a starting point and perform a detailed analysis of the dynamics inherent in the distinguished limit equation at this value of Ω^* . We caution, however, that, as with most forced, damped nonlinear oscillators, the largest resonant response occurs away from the resonance frequency of the linear oscillator. We use $\Omega^* = 1$ mainly as a starting point for the analysis, and the dynamics observed for a range of other Ω^* values is reported in section IV.

Some special cases of (14) can be readily analyzed when $\Omega^* = 1$. In the absence of forcing, *i.e.*, when $A = 0$, the phase portraits of (14) with $\zeta \geq 0$ are shown in figure 2. With no damping (figure 2a), the phase plane has a saddle point at $(1,0)$ and a center at $(0,0)$. The latter represents the equilibrium radius of the bubble which, when infinitesimally perturbed, results in simple harmonic oscillations of the bubble about that equilibrium. The saddle point at $(1,0)$ represents the effects of the second nearby root of the equation (5) which is an unstable equilibrium radius. When damping is added (figure 2b), the saddle point remains a saddle, but the center at $(0,0)$ becomes a stable spiral, attracting a well-defined region of the phase space towards itself. In the presence of weak forcing (small A) but with no damping ($\zeta = 0$), the behavior of (14) can be seen in a Poincaré section shown in figure 3.

III.1 Phase plane criterion for acoustic cavitation

To determine when a slightly subcritical bubble becomes unstable we choose a simple criterion based upon the phase portrait of the distinguished limit equation (14). For a given ζ , there exists a threshold value, A_{esc} , of A such that the trajectory through the origin $(0,0)$ grows without bound for $A > A_{\text{esc}}$, whereas that trajectory stays bounded for $A < A_{\text{esc}}$. A stable subcritical bubble becomes unstable as A increases past A_{esc} . Thus there is a stability curve in the (A, ζ) -plane separating the regions of this parameter space for which the trajectory starting at the origin in the phase-plane either escapes to infinity or remains bounded. Numerically, many such threshold ζ, A_{esc} pairs (represented by the open circles in figure 4) were found with $\Omega^* = 1$. The data are seen empirically to be well fitted by a least-squares straight line, given by $A_{\text{esc}} = 1.356\zeta + 0.058$.

For practical experimental purposes a linear regression curve based upon our escape criterion should provide a useful cavitation threshold for the acoustic pressure in the following dimensional form:

$$p_A > 3.835 \frac{\epsilon^{3/2} \sigma^{1/2} \mu}{\rho^{1/2} R_0^{3/2}} + 0.116 \frac{\epsilon^2 \sigma}{R_0}. \quad (16)$$

Here, ϵ is given by equation (8) and is itself a function of the equilibrium radius R_0 , surface tension σ and the pressure differential $p_0^\infty - p_v$.

III.2 Period doubling in the distinguished limit equation

It so happens that the stability curve for the trajectory of the origin can also be interpreted in terms of the period doubling route to chaos for the escape oscillator (14). In other words, the value of A_{esc} happens to be very near the limiting value at which the oscillations become chaotic, just before getting unbounded. For a fixed value of $\zeta > 0$ and a small enough A , the trajectory of the origin will settle upon a stable limit cycle in the phase plane. As A is increased gradually, the period of this stable limit cycle undergoes a doubling cascade as shown in figure 5 for a fixed value of $\zeta = 0.35$. The period doubling sequence will continue as A is increased until the trajectory of the origin eventually becomes chaotic, but still remains bounded. Finally, at a threshold value of A the trajectory of the origin will escape to infinity. This is the value of A that is given by the open circles on the stability diagram (figure 4). A typical bifurcation diagram for the escape oscillator (14) with $\zeta > 0$ is shown in figure 6 in which $\zeta = 0.375$.

III.3 Robustness of the simple cavitation criterion

In this subsection we justify defining a cavitation criterion based upon the fate of a single initial condition. In all simulations with $\zeta > 0$, there is a large region of initial conditions whose fate (escaping or staying bounded) is the same as that of the origin (figure 7). In fact, when the trajectory through the origin stays bounded it is clear from the simulations that the origin lies in the basin of attraction of a bounded, attracting periodic orbit, and points in a large region around it all lie in the basin of attraction of the same orbit. The trajectories through all points in that basin remain bounded. Then, as the forcing amplitude is increased the attractor is observed to undergo a sequence of period-doubling bifurcations, and this sequence culminates at the forcing magnitude when the origin and other initial conditions in a large region about it escape, because there is no longer a bounded attracting orbit in whose basin of attraction they lie.

III.4 Comparison with full Rayleigh-Plesset simulations

The stability threshold predicted by equation (16) can be compared to data obtained from simulating the Rayleigh-Plesset equation (13) directly. For small values of ϵ , figure 8 shows the resulting good agreement.

The following is a brief description of how the simulations were carried out. The material parameters used to produce figure 8 were $\rho = 998 \text{ kg/m}^3$, $\mu = 0.001 \text{ kg/m}\cdot\text{s}$, and $\sigma = 0.0725 \text{ N/m}$. Four values of ϵ were chosen, $\epsilon = 0.01, 0.05, 0.1$, and 0.2 . For each fixed value of ϵ and for a selected set of values of ζ ranging from 0 to 0.4, the parameters R_0 , R_{crit} , $(p_v - p_0^\infty)$, and Ω were calculated successively using the formulae:

$R_0 = 2\mu^2/(\zeta^2\epsilon\rho\sigma)$, $R_{\text{crit}} = R_0/(1-\epsilon/2)$, $p_v - p_0^\infty = (2\sigma/R_0)[1 - (1/3)/(1-\epsilon/2)^2]$, and $\Omega = [(2\sigma\epsilon)/(\rho R_0^3)]^{1/2}$. (Note that this succession of computations is done for each chosen value of ζ in each of the four plots.)

Having obtained the dimensional parameters required for the simulation of the full Rayleigh-Plesset equations corresponding to a given (ϵ, ζ) pair, we used a bisection procedure to determine A_{esc}^{RP} , the threshold value of A separating bounded and unbounded bubble trajectories. The bisection procedure was initiated by choosing a value of A close to the linear regression line. For this choice of A , the dimensional pressure, p_A , was calculated using the middle equation in (15). Then, the initial condition $R(0) = R_0$ and $\dot{R}(0) = 0$ was integrated forward in time using an *implicit* [22] fourth-order Runge-Kutta scheme. The adaptive, implicit scheme we used offers an accurate and stable means to integrate the governing equations. The time steps are large in those intervals in which the bubble radius does not change rapidly, and they are extremely short for the intervals where \dot{R} or \ddot{R} is large (see for example figure 4.7 on page 309 of [17]). If the bubble radius remained bounded during the simulation, then the value of A was increased slightly, a new p_A was calculated, and a new simulation was begun. If, on the other hand, the bubble radius became unbounded during the simulation, then the value of A was slightly decreased and a new simulation was initiated. Continuing with this bisection of A , the threshold value, A_{esc}^{RP} , where the bubble first becomes unstable was determined.

The dimensional counterpart (p_A -versus- R_0) to figure 8 is shown in figure 9 along with the dimensional stability curve given by equation (16). Note that for a given parameter ϵ , the relationship which defines the dimensionless damping parameter ζ , *i.e.*, $R_0 = 2\mu^2/(\zeta^2\epsilon\rho\sigma)$, can be thought of as defining the bubble radius R_0 . That is, for a given liquid viscosity μ and with all other physical parameters being constant, ζ can only change by varying the equilibrium radius R_0 . As such, the dimensionless A -versus- ζ curves can be put in terms of the dimensional p_A -versus- R_0 curves, drawn in figure 9.

To show the way in which the bubble radius actually becomes unbounded in the full Rayleigh-Plesset simulations, figure 10 provides the radius-versus-time plots for three typical simulations with the same value of $\zeta = 0.3$, where time is nondimensional. In this case, $A_{\text{esc}}^{RP} \approx 0.51$. The top two curves are obtained for values of A of 0.3 and 0.5, respectively. They show stable oscillations although a period-doubling can be seen to have occurred in going from one to the other. The bottom figure corresponds to $A = 0.53$ and shows that the bubble radius is becoming unbounded. The corresponding dimensional parameters for the Rayleigh-Plesset simulations are given in the figure caption.

III.5 Consistency of the distinguished limit equation

In this subsection, we argue, *a posteriori*, that it is self-consistent to use the escape oscillator as the distinguished limit equation (14) for the full Rayleigh-Plesset (13), *i.e.*, we show that the higher-order terms encountered during the change of variables from R to x may be neglected in a consistent fashion.

Recall that, in the derivation of the escape oscillator, all of the $\mathcal{O}(1)$ and $\mathcal{O}(\epsilon)$ terms dropped out, and the ordinary differential equation (14) was obtained by equating the terms of $\mathcal{O}(\epsilon^2)$. The remaining terms are of $\mathcal{O}(\epsilon^3)$ and higher. To be precise, at $\mathcal{O}(\epsilon^3)$, we find on the left-hand side:

$$x\ddot{x} - 2\zeta x\dot{x} + \frac{3}{2}\dot{x}^2,$$

and on the right-hand side:

$$-\frac{3}{4}x + 2x^2 - \frac{20}{3}x^3.$$

Moreover, we note that, for $i \geq 4$, all terms of $\mathcal{O}(\epsilon^i)$ on the left-hand side are of the form $x^{i-2}\dot{x}$, while all terms of $\mathcal{O}(\epsilon^i)$ on the right-hand side are polynomials in x .

We already know that, for trajectories of the escape oscillator that remain bounded, the x and \dot{x} variables stay $\mathcal{O}(1)$. Hence, all of the higher-order terms remain higher-order for these trajectories. Next, for trajectories that eventually escape (*i.e.*, those whose x -coordinate exceeds some large cut-off at some finite time), we know that x and \dot{x} are bounded until that time and afterwards they grow without bound. The fact that then R also grows without bound for these trajectories (due to the change of variables that defines x) is consistent with the dynamics of the full Rayleigh-Plesset equation.

Potential trouble could arise with trajectories for which x becomes negative and large in magnitude, *e.g.*, when $x \sim -1/\epsilon$ the coefficient of \ddot{x} vanishes. (This corresponds to small R .) A glance at the Poincaré map for the escape oscillator reveals, however, that trajectories which have $x \sim -1/\epsilon$ at some time τ can never have $x(\tau)$ and $\dot{x}(\tau)$ of $\mathcal{O}(1)$ simultaneously, for any τ . Hence, these trajectories are not in the regime of interest, neither for the escape oscillator nor for the full Rayleigh-Plesset equation. This completes the argument that it is self-consistent to use the escape oscillator for this study.

IV Pressure thresholds for general Ω^*

IV.1 Stability curves for various Ω^*

Until now, we have only examined the case $\Omega^* = 1$ in the distinguished limit equation (14). In this section we examine the dependence of the stability threshold on the acoustic frequency, Ω , for subcritical bubbles. Specifically, for frequencies Ω^* between 0.1 and 1.1, we performed numerical simulations of the distinguished limit equation (14) to determine many (ζ, A_{esc}) pairs. These pairs are plotted in figure 11, and the data points at each dimensionless frequency Ω^* are connected by straight lines (in contrast to the least squares fitting done in subsection III.1).

As in subsection III.1, good agreement between the distinguished limit equation threshold and the full Rayleigh-Plesset equation is observed for various values of Ω^* ; this can be seen in figure 12 which compares the two results at four different values of Ω^* given by 0.6, 0.7, 0.8 and 0.9, for a fixed value of $\epsilon = 0.05$.

Various features observed in figure 11, such as the flattening of these curves as Ω^* decreases, are explained in the next subsection.

IV.2 Minimum forcing threshold

Suppose that we wish to determine the driving frequency, for a given bubble with an equilibrium radius R_0 and a critical radius R_{crit} , so that the acoustic forcing amplitude necessary to make the bubble unstable is minimized. This can be done by choosing in figure 11, the value of Ω^* for which the corresponding threshold curve is below all the others for a given ζ . The result of such a procedure is provided in figure 13 as follows. Figure 13(a) provides the frequency of harmonic forcing at a given value of the damping parameter ζ for

which the required amplitude of the acoustic pressure field to create cavitation is the smallest. Figure 13(b) shows the dimensionless minimum pressure amplitude A_{esc} corresponding to the value of Ω^* just presented. In figure 13(a), for ζ between 0 and 0.225, the frequency curve is nearly a straight line and we fit a linear regression line to the data in that interval: $\Omega^* = -1.12\zeta + 0.90$ for $0 \leq \zeta \leq 0.225$. Correspondingly, in figure 13(b), we see that the minimum pressure curve is also nearly straight for the same interval of ζ values. The least squares line fitting the data in figure 13(b) is $A = 1.03\zeta + 0.02$ for $0 \leq \zeta \leq 0.225$.

When $\zeta = 0.225$, there is a discontinuity in the frequency curve, as seen in figure 13(a). At the same value of ζ , the pressure curve levels off to $A \approx 0.25$. This can be explained by a brief analysis of the normal form equation. The key observation will be that, in the escape oscillator with constant forcing (*i.e.*, constant right-hand side), there is a saddle-node bifurcation when the magnitude of the forcing is $1/4$. In order to carry out this brief analysis, we consider the cases $\zeta > 0$ and $\zeta = 0$ separately, beginning with $\zeta > 0$.

For $\zeta > 0$, the Poincaré map of the normal form equation (14) has an asymptotically stable fixed point (a sink), which corresponds to an attracting periodic orbit for the full normal form equation. Now, during each period of the external forcing, the location of this periodic orbit in the (x, \dot{x}) -plane changes. In fact, for the small values of Ω^* we are interested in here ($\Omega^* \leq 0.3$ approximately), the change in location occurs slowly, and one can write down a perturbation expansion for its position in powers of the small parameter Ω^* . The coefficients at each order are functions of the slow time $z \equiv \Omega^* t$. To leading order, *i.e.*, at $\mathcal{O}(1)$, the attracting periodic orbit is located at the point $(x(z), 0)$, where $x(z)$ is the smaller root of $x - x^2 = A \sin(z)$, namely

$$x(z) = \frac{1}{2} - \frac{1}{2}\sqrt{1 - 4A \sin(z)}.$$

Therefore, one sees directly that $A = 1/4$ is a critical value. In particular, if one considers any fixed value of $A < 1/4$, then the attracting periodic orbit exists for all time, and the trajectory of our initial condition $(0, 0)$ will be always be attracted to it. (Note that the viscosity $\zeta \geq 0.225$ is large enough so orbits are attracted to the stable periodic orbit at a faster rate than the rate at which the periodic orbit's position moves in the (x, \dot{x}) -plane due to the slow modulation.) However, for any fixed value of $A > 1/4$, the function giving $x(z)$ becomes complex after the slow time z reaches a critical value $z_*(A)$, where $A \sin(z_*) = 1/4$, and where we write $z_*(A)$ since z_* depends on A . Moreover, $x(z)$ remains complex in the interval $(z_*(A), \pi - z_*(A))$ during which $A \sin(z) > 1/4$. Viewed in terms of the slowly-varying phase portrait, the slowly-moving sink merges with the slowly-moving saddle in a saddle-node bifurcation when z reaches $z_*(A)$, and they disappear together for $z_*(A) < z < \pi - z_*(A)$. Hence, the attracting periodic orbit no longer exists when z reaches $z_*(A)$, and the trajectory that started at $(0, 0)$ — and that was spiraling in toward the slowly-moving attracting periodic orbit while z was less than $z_*(A)$ — escapes, because there is no longer any attractor to which it is drawn.

For the sake of completeness in presenting this analysis, we note that when $A = 1/4$, then $z_*(A) = \pi/2$; hence, it is precisely near this lowest value of A , namely $A = 1/4$, that we find the threshold for the acoustic forcing amplitude, and the escape happens near the slow time $z = \pi/2$. Moreover, for values of $A > 1/4$, $0 < z_*(A) < \pi/2$, and so the escape happens at an earlier time.

Numerically, the minimal frequency Ω^* appears to be $\Omega^* \approx 0$, where $\Omega^* = 0.01$ is the lowest value for which we conducted simulations. Moreover, this also explains why, as we see from figure 11 already, the

curves are flat with $A \approx 0.25$ for $\Omega^* \leq 0.3$. This is the range of small values of Ω^* for which the above analysis applies.

Next, having analyzed the regime in which $\zeta > 0$, we turn briefly to the case $\zeta = 0$. For small values, $\Omega^* \leq 0.3$, the curves in figure 11 remain flat near $A = 0.25$ all the way down to $\zeta = 0$. The full normal form equation with $\zeta = 0$ is a slowly-modulated Hamiltonian system. One can again use the slowly-varying phase planes as a guide to the analysis (although the periodic orbit is only neutrally stable when $\zeta = 0$ and no longer attracting as above), and the saddle-node bifurcation in the leading order problem at $A \sin(z_*) = 1/4$ is the main phenomenon responsible for the observation that the threshold forcing amplitude is near 0.25. (We also note that for a detailed analysis of the trapped orbits, one needs adiabatic separatrix-crossing theory, see [3], for example, but we shall not need that here.)

Finally, and most importantly, simulations of the full Rayleigh-Plesset equation confirm all the quantitative features of this analysis of the normal form equation. The open circles in figure 13 represent the numerically observed threshold forcing amplitudes, and these circles lie very close to the curves obtained as predictions from the normal form equation. We attribute this similarity to the fact that the phase portrait of the isothermal Rayleigh-Plesset equation has the same structure — stable and unstable equilibria, separatrix bounding the stable oscillations, and a saddle-node bifurcation when the forcing amplitude exceeds the threshold — as the normal form equation (see [26]).

IV.3 The dimensional form of the minimum forcing threshold

Recall, that for ζ between 0 and 0.225, we fit linear regression lines to portions of figures 13(a) and (b). Specifically, for figure 13(a) we found that, for a particular choice of ζ , the frequency which yields the smallest value of A_{esc} can be expressed as: $\Omega^* = -1.12\zeta + 0.90$ for $0 \leq \zeta \leq 0.225$. And for figure 13(b) we found that the stability boundary for the minimum forcing is given by,

$$A = \begin{cases} 1.03\zeta + 0.02 & \text{for } 0 \leq \zeta \leq 0.225 \\ 0.25 & \text{for } 0.225 \leq \zeta \leq 0.4. \end{cases} \quad (17)$$

Using the definitions of ζ , A and Ω^* as given by (15), the “optimal” acoustic frequency to cause cavitation of a subcritical bubble is given in dimensional form by

$$\Omega = -2.24 \frac{\mu}{\rho R_0^2} + 1.27 \frac{\epsilon^{1/2} \sigma^{1/2}}{\rho^{1/2} R_0^{3/2}} \quad \text{for } 0 \leq \left(\frac{2\mu^2}{\sigma \epsilon \rho R_0} \right)^{1/2} \leq 0.225.$$

Correspondingly, the minimum acoustic pressure threshold is

$$p_A > \begin{cases} 2.91 \frac{\epsilon^{3/2} \sigma^{1/2} \mu}{\rho^{1/2} R_0^{3/2}} + 0.04 \frac{\epsilon^2 \sigma}{R_0} & \text{for } 0 \leq \left(\frac{2\mu^2}{\sigma \epsilon \rho R_0} \right)^{1/2} \leq 0.225 \\ \frac{\epsilon^2 \sigma}{2R_0} & \text{for } 0.225 \leq \left(\frac{2\mu^2}{\sigma \epsilon \rho R_0} \right)^{1/2} \leq 0.4. \end{cases}$$

IV.4 A lower bound for A_{esc} via Melnikov analysis

The distinguished limit equation (14) can be written as the perturbed system

$$\dot{\mathbf{x}} = \mathbf{f}(\mathbf{x}) + \tilde{\epsilon} \mathbf{g}(\mathbf{x}, \tau)$$

where, $\mathbf{x} = (x, y)$, $\mathbf{f}(x, y) = (y, x^2 - x)$ and $\mathbf{g}(x, y, \tau) = (0, \bar{A} \sin(\Omega^* \tau) - 2\bar{\zeta}y)$ with $A = \tilde{\epsilon}\bar{A}$, $\zeta = \tilde{\epsilon}\bar{\zeta}$. When $\tilde{\epsilon} = 0$ the system has a center at $(0,0)$ and a saddle point at $(1,0)$. The homoclinic orbit to the unperturbed saddle is given by $\gamma_0(\tau) = (x(\tau), y(\tau))$ where $x(\tau) = -(1/2) + (3/2) \tanh^2(\tau/2)$ and $y(\tau) = (3/2) \tanh(\tau/2) \operatorname{sech}^2(\tau/2)$. Following [12], the Melnikov function takes the form

$$\begin{aligned} M(\tau_0) &= \int_{-\infty}^{\infty} \mathbf{f}(\gamma_0(\tau)) \wedge \mathbf{g}(\gamma_0(\tau), \tau + \tau_0) d\tau \\ &= \frac{3}{2} \bar{A} \int_{-\infty}^{\infty} \sin[\Omega^*(\tau + \tau_0)] \tanh\left(\frac{\tau}{2}\right) \operatorname{sech}^2\left(\frac{\tau}{2}\right) d\tau \\ &\quad - \frac{9}{2} \bar{\zeta} \int_{-\infty}^{\infty} \tanh^2\left(\frac{\tau}{2}\right) \operatorname{sech}^4\left(\frac{\tau}{2}\right) d\tau. \end{aligned}$$

The first integral can be done with a residue calculation, and the second integral is evaluated in a straightforward manner, resulting in:

$$M(\tau_0) = - \left[\frac{6\pi(\Omega^*)^2 \cos(\Omega^*\tau_0)}{\sinh(\pi\Omega^*)} \right] \bar{A} - \frac{12}{5} \bar{\zeta}.$$

The Melnikov function has simple zeros when $\bar{A} > \bar{A}_{\text{h.tan.}}$, where

$$\bar{A}_{\text{h.tan.}} = \left(\frac{2 \sinh(\pi\Omega^*)}{5\pi(\Omega^*)^2} \right) \bar{\zeta}. \quad (18)$$

Hence the stable and unstable manifolds of the perturbed saddle point intersect transversely for all sufficiently small $\tilde{\epsilon} \neq 0$ when $\bar{A} > \bar{A}_{\text{h.tan.}}$ [12]. The resulting chaotic dynamics is evident in figure 5, for example. Since homoclinic tangency must occur before the trajectory through the origin can escape, $\bar{A}_{\text{h.tan.}}$ may be viewed as a precursor to A_{esc} . Figure 14 demonstrates that, for small enough $\tilde{\epsilon}$, equation (18) provides a lower bound for the stability curves seen in figure 11.

The reason why Melnikov analysis yields a lower bound for the cavitation threshold relates to how deeply the stable and unstable manifolds of the saddle fixed point of the Poincare map for equation (14) penetrate into the region bounded by the separatrix in the $A, \zeta = 0$ case. For sufficiently small values of $\tilde{\epsilon}$, long segments of the perturbed local stable and unstable manifolds will stay $\mathcal{O}(\tilde{\epsilon})$ close to the unperturbed homoclinic orbit. However, as $\tilde{\epsilon}$ grows (and one gets out of the regime in which the asymptotic Melnikov theory strictly applies), these local manifolds will penetrate more deeply into the region bounded by the separatrix in the $A, \zeta = 0$ case. In fact, there is a sizable gap in the parameter space between the homoclinic tangency values and the escape values corresponding to our cavitation criteria, *i.e.*, when the trajectory through the origin grows without bound. There is a similar gap when other initial conditions are chosen.

The Melnikov function was also calculated in [27]. There, a detailed analysis of escape from a cubic potential is described and the fractal basin boundaries and occurrence of homoclinic tangencies are given. We also refer the reader to [11] in which a closely related second order, damped and driven oscillator with quadratic nonlinearity is studied using both homoclinic Melnikov theory, as was done here, and subharmonic Melnikov theory. The existence of periodic orbits is demonstrated there, and period doubling bifurcations of these periodic orbits are examined. Their equation arises from the study of travelling waves in a forced, damped KdV equation.

V Pressure fields with two fast frequencies

In this section, we consider what happens to the cavitation threshold if two fast frequency components are present in the acoustic pressure field, and the slow transducer, which lowers the ambient pressure and whose effect is quasistatic, is also still present. In figure 15, we show the results from simulations with quasiperiodic pressure fields. These were obtained from simulations of (14) with the forcing replaced by $(A/2)(\sin(\Omega_1^*\tau) + \sin(\Omega_2^*\tau))$, and a wide range of values for Ω_1^* and Ω_2^* . For a fixed value of $\zeta = 0.25$, the cavitation surface shown in the figure was plotted by computing the triples $(\Omega_1^*, \Omega_2^*, A_{\text{esc}})$.

We note that in figure 15, the intersection of the cavitation surface and the vertical plane given by $\Omega_1^* = \Omega_2^*$ represents cavitation thresholds for acoustic forcing of the form $A \sin(\Omega^*\tau)$ (*i.e.*, a single fast frequency component and a quasistatic component). Furthermore, we see that the global minimum of the cavitation surface lies along the line $\Omega_1^* = \Omega_2^*$. Hence, for $A/2$ as our particular choice of quasiperiodic forcing coefficient, the addition of a second fast frequency component in the pressure field does not lower the cavitation threshold beyond that of the single fast frequency case.

VI Discussion

A distinguished limit equation has been derived which is suitable for use in determining cavitation events of slightly subcritical bubbles. This “normal form” equation allows us to study cavitation thresholds for a range of acoustic forcing frequencies. For $\Omega^* = 1$, we find an explicit expression for the cavitation threshold via linear regression, since the simulation data reveal an approximate linear dependence of the nondimensional threshold amplitude, A , on the nondimensional liquid viscosity, ζ . When converted to dimensional form, this linear expression translates into a nonlinear dependence, cf. equation (16), on the material parameters. In all of our simulations, the acoustic threshold amplitude coincides with the amplitudes at which the cascades of period-doubling subharmonics terminate.

Particular attention has also been paid to calculating the frequency, Ω^* , at which a given subcritical bubble will most easily cavitate. Expression (17) for the corresponding minimum threshold amplitude A grows linearly in ζ for $\zeta < 0.225$ until the critical amplitude $A = 1/4$ is reached, and the threshold amplitude stays constant at $A \approx 1/4$ for larger ζ . For these larger values of $\zeta > 0.225$, the “optimal” frequency is essentially zero, as we showed by doing a slowly-varying phase portrait analysis and exploiting the fact that the normal form equation undergoes a saddle-node bifurcation at $A = 1/4$ in which the entire region of bounded stable orbits vanishes. The full Rayleigh-Plesset equation undergoes a similar bifurcation at forcing amplitudes very near $A = 1/4$ for sufficiently small ϵ . Overall, the results from the normal form equation are in excellent agreement with those of the full Rayleigh-Plesset equation, and this may be attributed to the high level of similarity between the phase-space structures of both equations.

In view of the findings in [26], we may draw an additional conclusion from the present work. In a certain sense, we have extended the finding of lowered transition amplitudes reported in [26] to the limiting case of one low frequency and one fast frequency. We find that if a low frequency transducer prepares a bubble to become slightly subcritical, then the presence of a high frequency transducer can lower the cavitation

threshold of the bubble below the Blake threshold.

Our results on the optimum forcing frequency and minimum pressure threshold to cavitate a subcritical bubble may also be useful in fine-tuning experimental work on single-bubble sonoluminescence (SBSL). In SBSL [10, 6, 23], a single bubble is acoustically forced to undergo repeated cavitation/collapse cycles, in each of which a short-lived flash of light is produced. While the process through which a collapsing bubble emits light is very complex and involves many nonlinear phenomena, the possibility of better control over cavitation and collapse, *e.g.*, through the use of multiple-frequency forcing, can perhaps be investigated using the type of analysis presented in this paper.

Acknowledgments — We are grateful to Professor S. Madanshetty for many helpful discussions. The authors would also like to thank the referees for their comments. This research was made possible by Group Infrastructure Grant DMS-9631755 from the National Science Foundation. A.H. gratefully acknowledges financial support from the National Science Foundation via this grant. T.K. gratefully acknowledges support from the Alfred P. Sloan Foundation in the form of a Sloan Research Fellowship.

Appendix: Coaxing experiments in acoustic microcavitation

To illustrate one application of our results, we now briefly consider the experimental findings of [18] on so-called “coaxing” of acoustic microcavitation. In these experiments, smooth submicrometer spheres were added to clean water and were found to facilitate the nucleation of cavitation events (*i.e.* reduce the cavitation threshold) when a high-frequency transducer (originally aimed as a detector) was turned on at a relatively low pressure amplitude. Specifically, the main cavitation transducer was operating at a frequency of 0.75 MHz, while the active detector had a frequency of 30 MHz. In a typical experiment, with 0.984-micron spheres added to clean water, the cavitation threshold in the absence of the active detector was found to be about 15 bar peak negative. When the active detector was turned on, producing a minimum pressure of only 0.5 bar peak negative by itself, it caused the cavitation threshold of the main transducer to be reduced from 15 to 7 bar peak negative. The polystyrene latex spheres were observed under scanning electron microscopes and their surface was determined to be smooth to about 50 nanometers. It was thus thought that any gas pockets which were trapped on their surface due to incomplete wetting and which served as nucleation sites for cavitation, were smaller in size than this length. In [18], it is conjectured that the extremely high fluid accelerations created by the high-frequency active detector, coupled with the density mismatch between the gas and the liquid, caused these gas pockets to accumulate on the surface of the spheres and form much larger “gas caps” (on the order of the particle size), which then cavitated at the lower threshold. Here we attempt to provide an alternative explanation for the observed lowering of the threshold in the presence of the active detector.

To effect our estimates, we shall use the same physical parameters as earlier: $\mu = 0.001 \text{ kg/m}\cdot\text{s}$, $\rho = 0.998 \text{ kg/m}^3$ and $\sigma = 0.0725 \text{ N/m}$. We also ignore the vapor pressure of the liquid at room temperature. Note also that $1 \text{ bar} = 10^5 \text{ N/m}^2$ and that the transducer frequencies f cited above are related to the radian frequencies

Ω used earlier by $\Omega = 2\pi f$.

Let us begin by estimating a typical size for the nucleation sites which cavitate at $p_{L\text{crit}} = -15$ bar in the absence of the active detector. Upon using Blake's classical estimate of $p_{L\text{crit}} = -0.77\sigma/R_0$, the equilibrium radius of the trapped air pockets is estimated to be $R_0 = 3.7 \times 10^{-8}$ m or 37 nm. This size is consistent with the observation that the surfaces of the spheres were smooth to within 50 nm. We note that such a small cavitation nucleus cannot exist within the homogeneous liquid itself since it would dissolve away extremely fast due to its overpressure resulting from surface tension. However, when trapped in a crevice or within the roughness on solid surfaces, it can be stabilized against dissolution with the aid of the meniscus shape which separates it from the liquid. The natural frequency of a 37 nm bubble (if it were spherical) found from equation (12) would be 385 MHz which is very large compared to forcing frequency of the cavitation transducer which is 0.75 MHz. Therefore, consistent with Blake's classical criterion, the pressure changes in the liquid would appear quasistatic to the bubble and at such a small size, surface tension does dominate the bubble dynamics. The Blake critical radius R_{crit} which corresponds to this equilibrium radius R_0 of 37 nm can be calculated to be $R_{\text{crit}} = 64$ nm.

Let us now suppose that the cavitation transducer is operating at $p_L = -7$ bar peak negative as in the experiments with the active transducer also turned on. Using equation (5), the final expanded radius of the bubble when the liquid pressure is quasistatically reduced to -7 bar is found to be 4.2×10^{-8} m or 42 nm. In other words, a bubble of original radius 37 nm at a liquid pressure of 1 bar, grows to a maximum size of 42 nm when the liquid pressure is reduced to -7 bar. Its critical radius is still 64 nm, reached if the liquid pressure were to be reduced further to -15 bar.

At this point, since the pressure changes in the liquid due to the 0.75 MHz cavitation transducer are occurring slowly compared both with the natural timescale of the bubble and the 30 MHz detector, let us take the mean pressure in the liquid to be the $p_0^\infty = -7$ bar, and imagine the bubble size at this pressure to be its new equilibrium radius $R_0 = 42$ nm, with the critical radius still given by $R_{\text{crit}} = 64$ nm. This bubble is now assumed to be forced by the 30 MHz transducer at an acoustic pressure amplitude of 1.5 bar (*i.e.* -0.5 bar peak negative). Using these values, the perturbation parameter ϵ is calculated from equation (8) to be $\epsilon = 0.69$. This parameter is too big for the results of the asymptotic theory to provide meaningful quantitative agreement; nevertheless, we proceed with the discussion to see if we can at least obtain the right order of magnitude for the pressure threshold.

With the given physical parameters, and using the forcing pressure of $p_A = 1.5$ bar and $\Omega = 2\pi \times 30 \times 10^{-6}$ s $^{-1}$, the parameters ζ , A and Ω^* are calculated from equation (15) to be: $\zeta = 0.98$, $A = 0.09$ and $\Omega^* = 0.16$. Upon examining figure 13, at the relatively large damping parameter $\zeta = 0.98$ (beyond the range originally considered) the minimum forcing threshold would appear to correspond to the constant value of $A = 0.25$. Here we also note that this same forcing threshold is also observed with a range of small Ω^* , including $\Omega^* = 0.16$, see figure 11. In other words, the predicted threshold pressure for the active detector to cause cavitation is $A = 0.25$ which corresponds roughly to $p_A = 4$ bar, whereas in the experiments the threshold was seen to be $A = 0.09$ or $p_A = 1.5$ bar. Despite the lack of quantitative agreement, the theoretical predictions and the experiments do show the same trends. Namely, in the absence of the 30-MHz detector, the pressure in the liquid had to be reduced to -15 bar for cavitation to occur. With the high-frequency transducer

turned on, however, cavitation occurred at a minimum pressure of $-7 - 1.5 = -8.5$ bar in the experiments and at $-7 - 4 = -11$ bar based on the theory. (We are adding the negative pressure contribution from the two transducers to arrive at the final minimum pressure). Thus, the presence of the second high-frequency transducer does reduce the pressure threshold for cavitation in both cases.

References

- [1] R.E. Apfel, Some New results on cavitation threshold prediction and bubble dynamics, in *Cavitation and Inhomogeneities in Underwater Acoustics*, Springer Series in Electrophysics, v.4, W. Lauterborn (ed.), 79–83 (Springer, Berlin, 1980).
- [2] F.G. Blake, Technical Memo 12, Acoustics Research Laboratory, Harvard University, Cambridge, MA (1949).
- [3] J.R. Cary, D.F. Escande and J. Tennyson, Adiabatic invariant change due to separatrix crossing, *Phys. Rev. A* **34**, 4256–4275 (1986).
- [4] H.-C. Chang and L.-H. Chen, Growth of a gas bubble in a viscous fluid *Phys. Fluids* **29**, 3530–3536 (1986).
- [5] L.A. Crum, Acoustic cavitation thresholds in water, in *Cavitation and Inhomogeneities in Underwater Acoustics*, Springer Series in Electrophysics, v.4, W. Lauterborn (ed.), 84–87 (Springer, Berlin, 1980).
- [6] L.A. Crum, Sonoluminescence, *Physics Today*, 22–29 (1994).
- [7] C. Dugué, D.H. Fruman, J.-Y. Billard and P. Cerrutti, Dynamic criterion for cavitation of bubbles, *J. Fluids Engineering* **114**(2), 250–254 (1992).
- [8] R. Esche, Untersuchung der Schwingungskavitation in Fluessigkeiten, *Acustica* **2**, AB208–AB218 (1952).
- [9] Z.C. Feng and L.G. Leal, Nonlinear bubble dynamics, *Ann. Rev. Fluid Mech.* **29**, 201–243 (1997).
- [10] D.F. Gaitan, L.A. Crum, C.C. Church and R.A. Roy, Sonoluminescence and bubble dynamics for a single, stable, cavitation bubble, *J. Acoust. Soc. Am.*, **91**, 3166–3183 (1992).
- [11] R. Grimshaw and X. Tian, Periodic and chaotic behavior in a reduction of the perturbed KdV equation, *Proc. R. Soc. Lond. A* **445**, 1–21 (1994).
- [12] J. Guckenheimer and P. Holmes, *Nonlinear Oscillations, Dynamical Systems, and Bifurcations of Vector Fields*, (Applied Mathematical Sciences 42, Springer-Verlag, New York, 1993).
- [13] I.S. Kang and L.G. Leal, Bubble dynamics in time-periodic straining flows, *J. Fluid Mech.* **218**, 41–69 (1990).
- [14] W. Lauterborn, Numerical investigation of nonlinear oscillations of gas bubbles in liquids, *J. Acoust. Soc. Am.* **59**, 283–293 (1976).
- [15] W. Lauterborn and A. Koch, Holographic observation of period-doubled and chaotic bubble oscillations in acoustic cavitation, *Phys. Rev. A* **35**(4), 1974–1976 (1987).
- [16] L.G. Leal, *Laminar Flow and Convective Transport Processes* (Butterworth-Heinemann Series in Chemical Engineering, Boston, 1992).
- [17] T.G. Leighton, *The Acoustic Bubble* (Academic Press Inc., San Diego, 1994).

- [18] S.I. Madanshetty, A conceptual model for acoustic microcavitation, *J. Acoust. Soc. Am.* **98**, 2681–2689 (1995).
- [19] Y. Matsumoto and A.E. Beylich, Influence of homogeneous condensation inside a small gas bubble on its pressure response, *J. Fluids Engineering* **107**, 281–286 (1985).
- [20] U. Parlitz, V. Englisch, C. Scheffczyk, and W. Lauterborn, Bifurcation structure of bubble oscillators, *J. Acoust. Soc. Am.* **88**, 1061–1077 (1990).
- [21] M.S. Plesset and A. Prosperetti, Bubble dynamics and cavitation, *Ann. Rev. Fluid Mech.* **9**, 145–185 (1977).
- [22] W. Press, W. Vetterling, S. Teukolsky and B. Flannery, *Numerical Recipes in C - The Art of Scientific Computing, 2nd ed.*, (Cambridge University Press, 1992).
- [23] S.J. Puterman, Sonoluminescence: sound into light, *Scientific American*, **272**, 46–51 (1995).
- [24] Y. Sato and A. Shima, The growth of bubbles in viscous incompressible liquids, *Report of Inst. of High Speed Mechanics*, number 40-319, 23–49 (1979).
- [25] P. Smereka, B. Birnir and S. Banerjee, Regular and chaotic bubble oscillations in periodically driven pressure fields, *Phys. Fluids* **30**, 3342–3350 (1987).
- [26] A.J. Szeri and L.G. Leal, The onset of chaotic oscillations and rapid growth of a spherical bubble at subcritical conditions in an incompressible liquid, *Phys. Fluids A* **3**, 551–555 (1991).
- [27] J.M.T. Thompson, Chaotic phenomena triggering the escape from a potential well, *Proc. R. Soc. Lond. A* **421**, 195–225 (1989).

Figure Captions

Figure 1: Pressure in the liquid, p_L , versus bubble radius, R , as governed by equation (5).

Figure 2: Phase portraits for the distinguished limit equation (14). In (a), $A = 0$ and $\zeta = 0$. The fixed point $(0,0)$ is a center. The fixed point $(1,0)$ is a saddle. In (b), $A = 0$ and $\zeta = 0.09$. The fixed point $(0,0)$ is a stable spiral.

Figure 3: Poincaré section showing the unstable manifold of the saddle fixed point $(0.999769375, -0.024007197)$ for $A = 0.048$ and $\zeta = 0$. Asymptotically, the saddle point is located at a distance $\mathcal{O}(A)$ from $(1,0)$, specifically $(1 - A^2/10 + \mathcal{O}(A^4), -A/2 - (13/200)A^3 + \mathcal{O}(A^5))$. Invariant tori are shown inside a portion of the unstable manifold. The center point has moved a large distance from $(0,0)$ in this case due to the 1:1 resonance when $\Omega^* = 1$. And we note for comparison that with nonresonant values of Ω^* , Poincaré sections show that the center only moves an $\mathcal{O}(A)$ distance. For example, when $\Omega^* = 0.6, 0.7, 0.85$, the centers are located approximately at the points $(0.009, 0.045), (0.009, 0.066)$ and $(0.029, 0.163)$ respectively.

Figure 4: Escape parameters for the trajectory of the origin $(0,0)$. For values of A, ζ above the regression line the trajectory of the origin grows without bound. Below this line the trajectory of the origin remains bounded. Least squares fit: $A = 1.356\zeta + 0.058$.

Figure 5: Period doubling route to chaos in the distinguished limit equation (14). For $\zeta = 0.35$, the limit cycles undergo period doubling as A is increased.

Figure 6: Bifurcation diagram ($\zeta = 0.375$). Plotted is \dot{x} versus A . For each fixed value of A , the origin $(0,0)$ is integrated numerically and the value of \dot{x} is plotted every $\Delta\tau = 2\pi$.

Figure 7: Bounded trajectories for the distinguished limit equation with $\zeta = 0.2$, $A = 0.3$ and $\Omega^* = 1.0$. The dark region is the set of initial conditions whose trajectories remain bounded; it is the basin of attraction of the periodic orbit that exists in the period-doubling hierarchy for this value of A .

Figure 8: Simulations of the full Rayleigh-Plesset equation for four different values of ϵ . Each open circle represents an (A, ζ) pair at which the bubble first goes unstable. Superimposed is the linear regression line obtained from the simple criterion based upon the distinguished limit equation. In (a)–(d), $\epsilon = 0.01, 0.05, 0.1, 0.2$, respectively.

Figure 9: Simulations of the full Rayleigh-Plesset equation for four different values of ϵ . Each open circle represents a (p_A, R_0) pair at which the bubble first goes unstable. Superimposed is the threshold curve (16) obtained from the simple criterion based upon the distinguished limit equation. In (a)–(d), $\epsilon = 0.01, 0.05, 0.1, 0.2$, respectively.

Figure 10: Radius versus time plots ($\epsilon = 0.1, \zeta = 0.3, A = 0.3, 0.5, 0.53$).

Dimensional parameters: $R_0 = 3.0 \mu\text{m}$, $R_{crit} = 3.2 \mu\text{m}$, $p_v - p_0^\infty = 29.7 \text{ kPa}$, $\Omega = 0.7 \text{ MHz}$.

Top: $p_A = 141.6 \text{ Pa}$. Middle: $p_A = 236.0 \text{ Pa}$. Bottom: $p_A = 250.2 \text{ Pa}$.

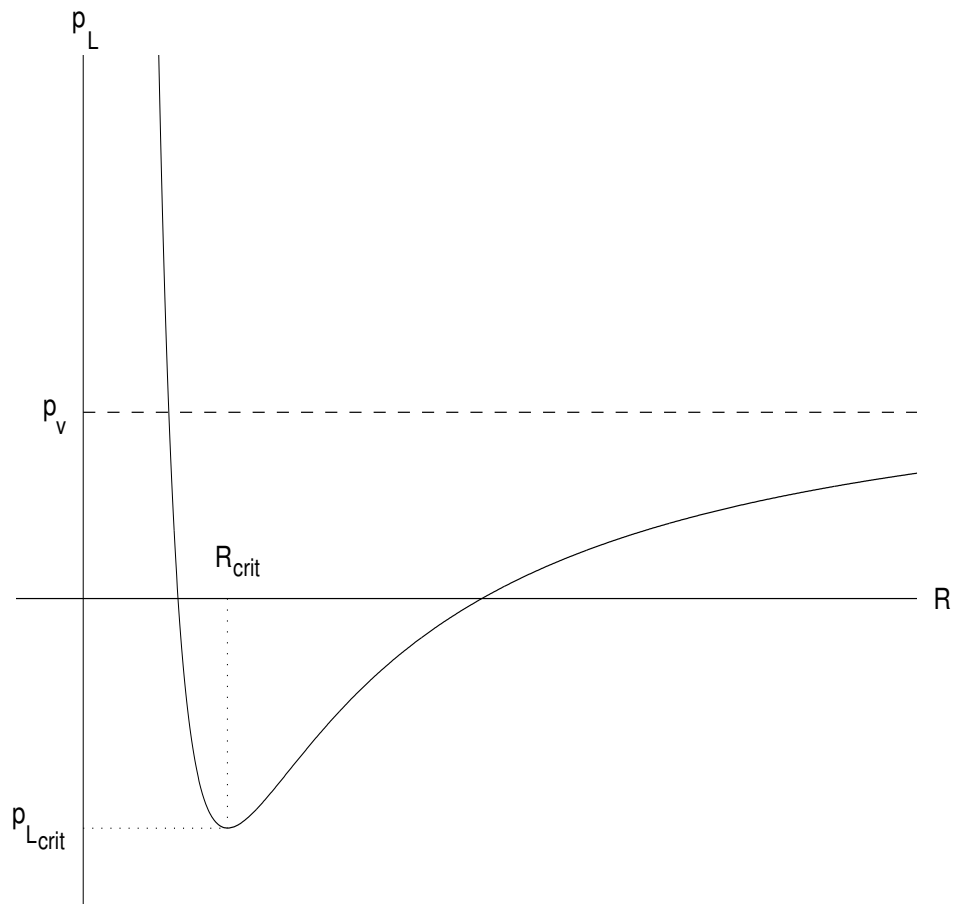
Figure 11: Stability threshold curves for the origin trajectory of the distinguished limit equation (14) for many different values of Ω^* . The values of Ω^* on the right hand border label the different threshold curves.

Figure 12: Simulations of the full Rayleigh-Plesset equation for four different values of Ω^* . In each plot $\epsilon = 0.05$. Each open circle represents an A, ζ pair at which the bubble first goes unstable. Superimposed is the threshold curve obtained from the distinguished limit equation. In (a)–(d), $\Omega^* = 0.6, 0.7, 0.8, 0.9$, respectively.

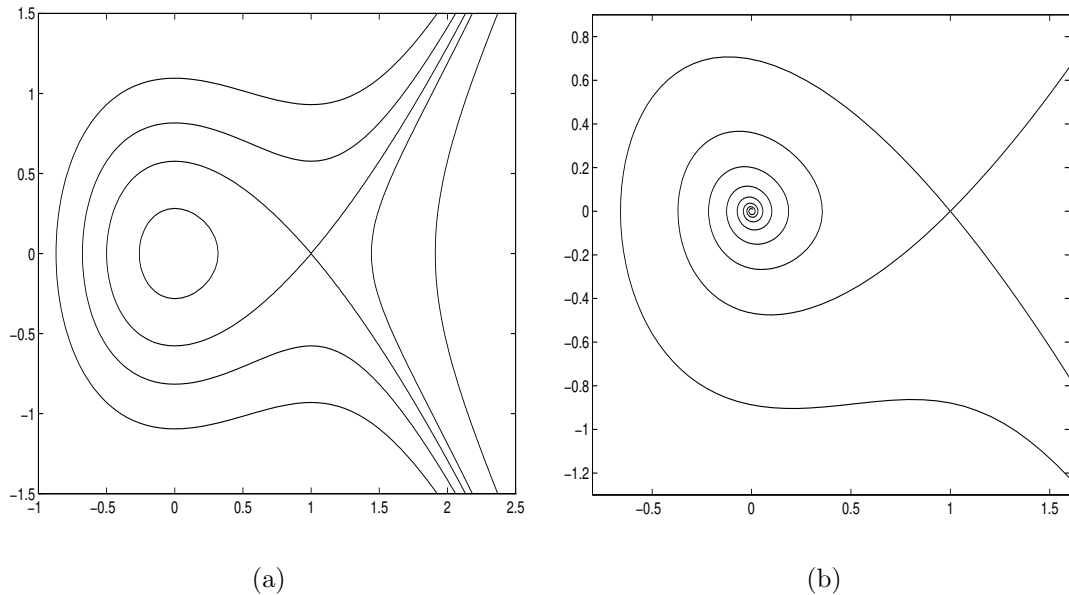
Figure 13: In (a), the Ω^* that minimizes A_{esc} is plotted versus ζ . In (b), the minimum value of A_{esc} corresponding to the value of Ω^* in (a) is plotted versus ζ . The open circles represent Rayleigh-Plesset calculations of the minimum threshold with $\epsilon = 0.05$.

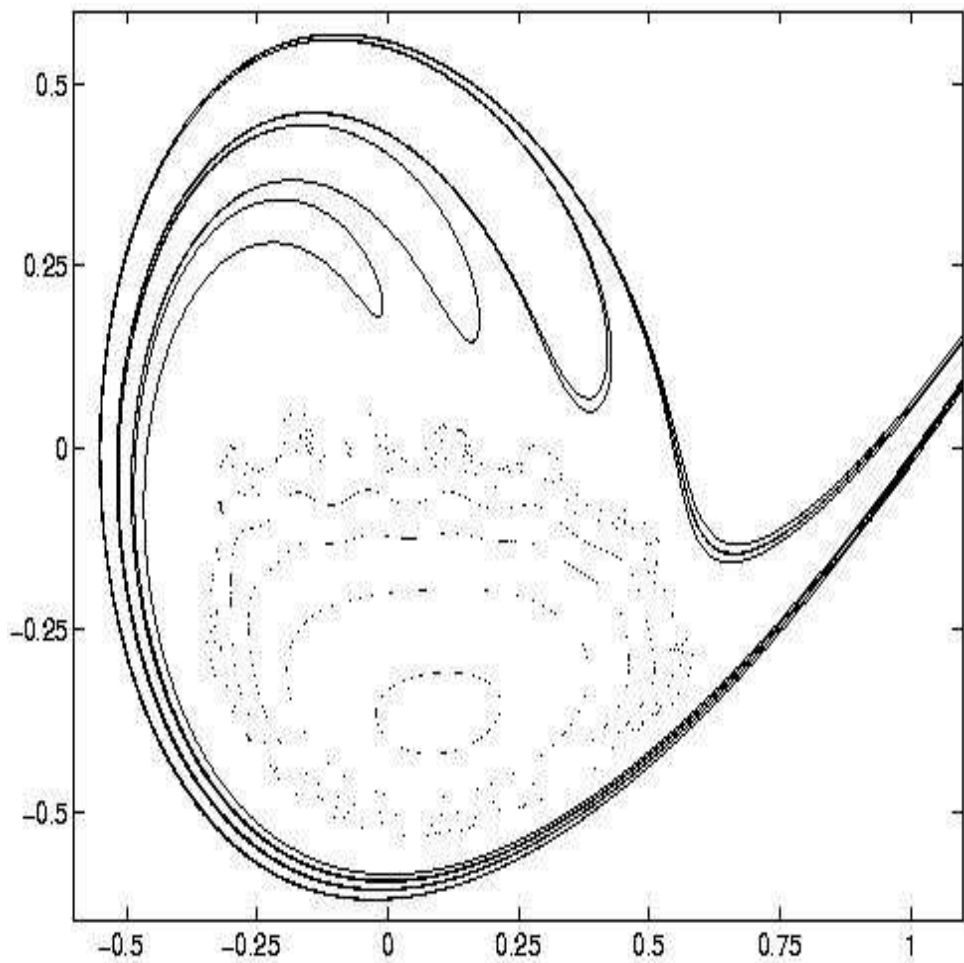
Figure 14: Comparisons of the stability curves of figure 11 with the Melnikov analysis for two values of Ω^* . The dotted line is the stability curve obtained from the distinguished limit equation. The solid straight line is equation (18). In (a) and (b), $\Omega^* = 0.9, 1.1$, respectively.

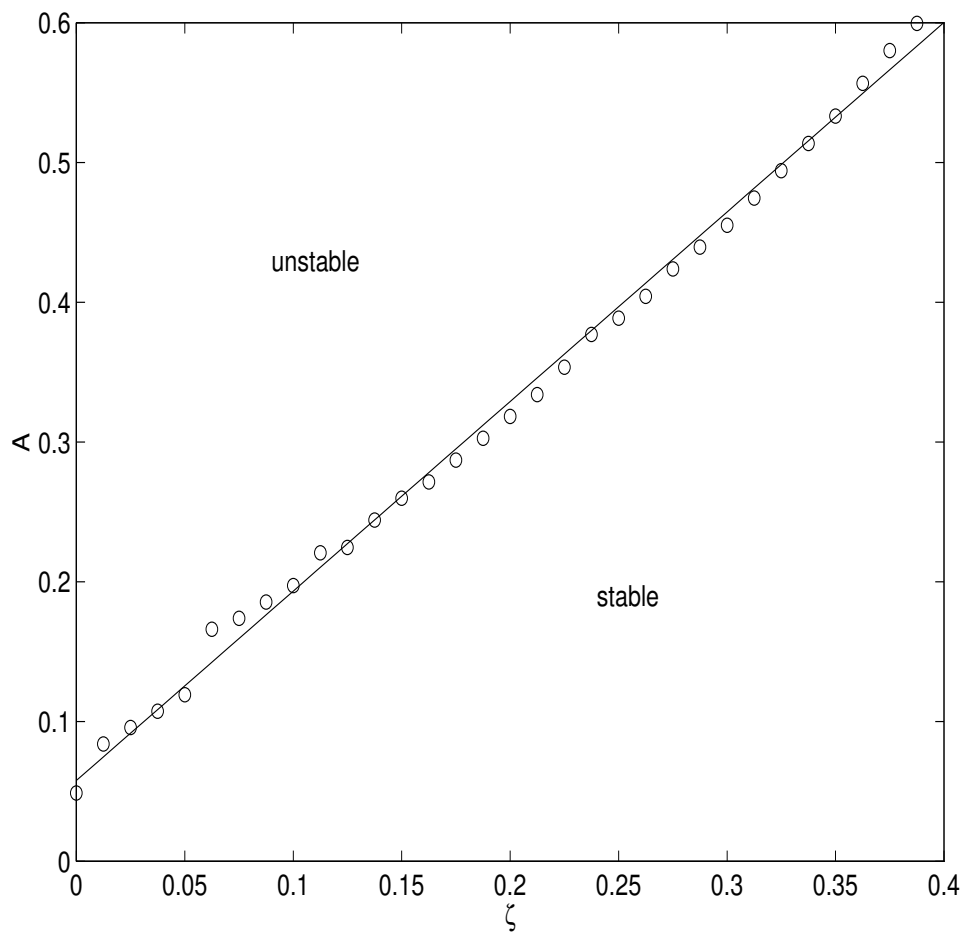
Figure 15: Stability threshold surface for the trajectory through the origin obtained by integrating the distinguished limit equation with quasiperiodic forcing. This was obtained from simulations of (14) with the forcing replaced by $(A/2)(\sin(\Omega_1^*\tau) + \sin(\Omega_2^*\tau))$, and for $0 < \Omega_1^*, \Omega_2^* < 1.3$. The value of ζ was fixed at $\zeta = 0.25$. The points below the surface correspond to parameter values for which the trajectory of the origin remains bounded whereas those points above the surface are parameters which lead to an escape trajectory for the origin. Qualitatively and quantitatively similar results were obtained for $\zeta = 0.15$ and $\zeta = 0.35$.



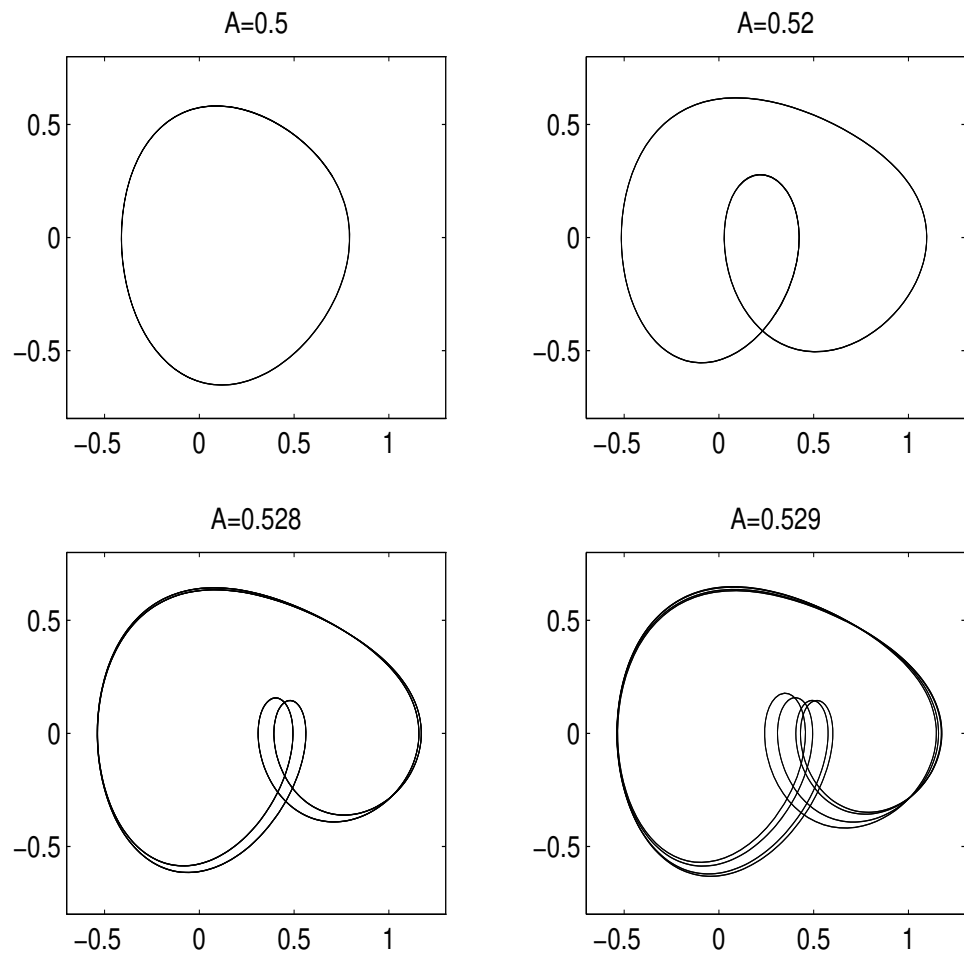
PF#1091, Harkin, Nadim and Kaper – Figure 2



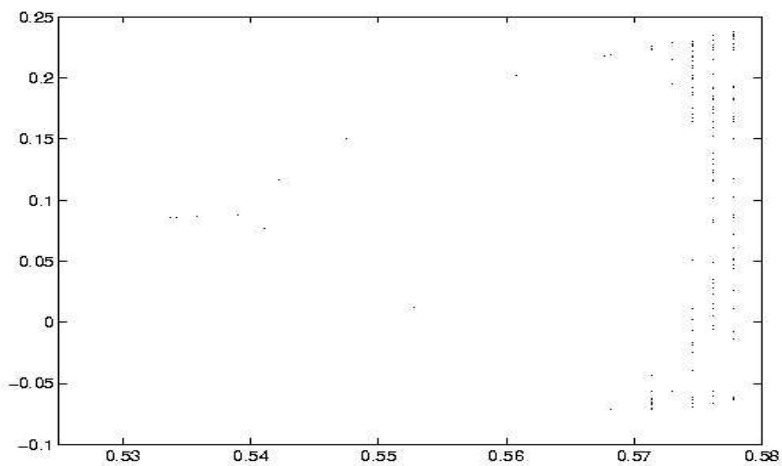




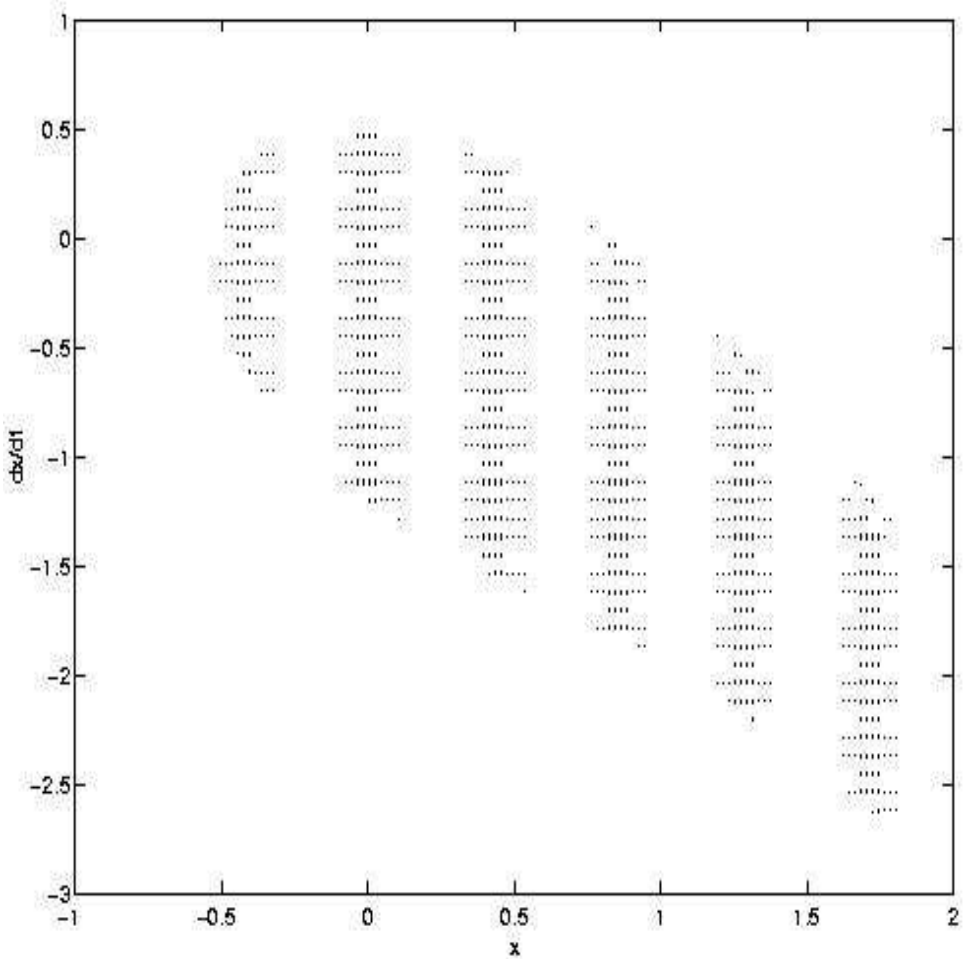
PF#1091, Harkin, Nadim and Kaper – Figure 5



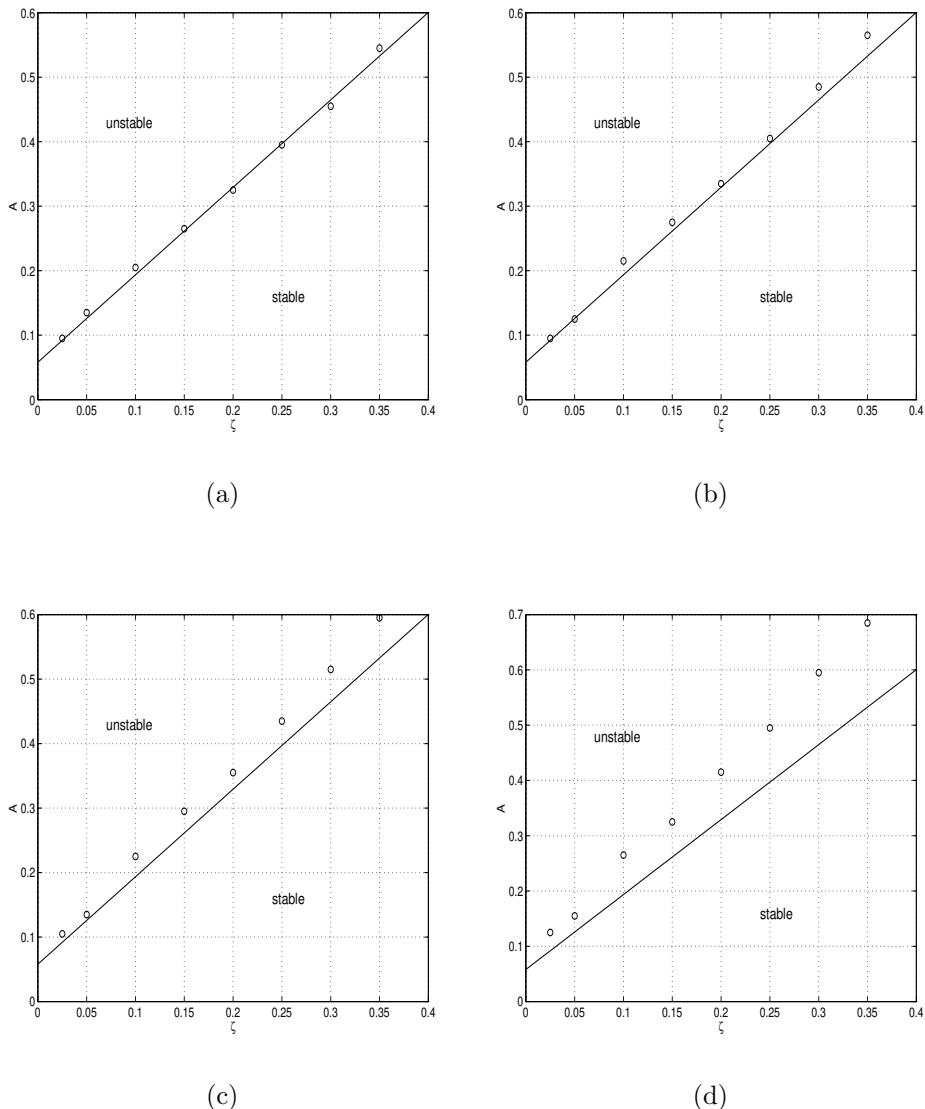
PF#1091, Harkin, Nadim and Kaper – Figure 6



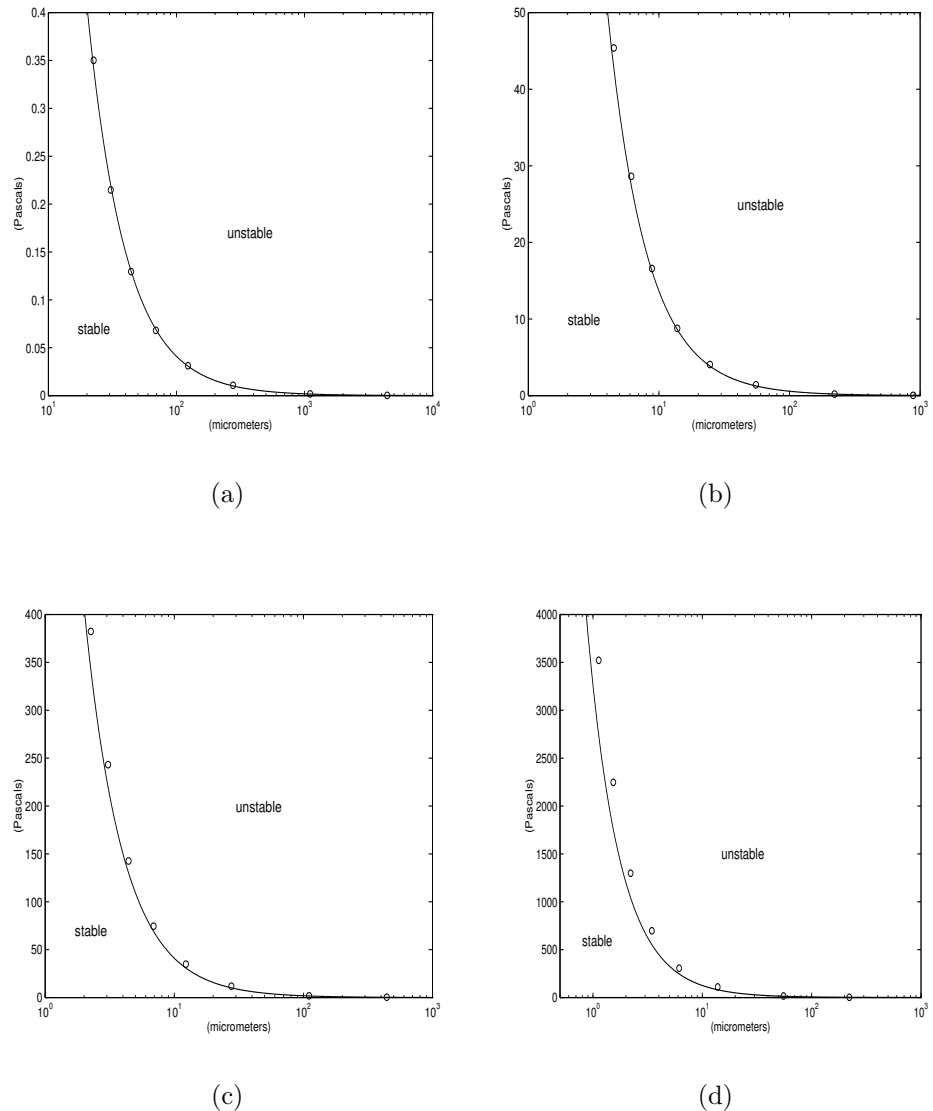
PF#1091, Harkin, Nadim and Kaper – Figure 7



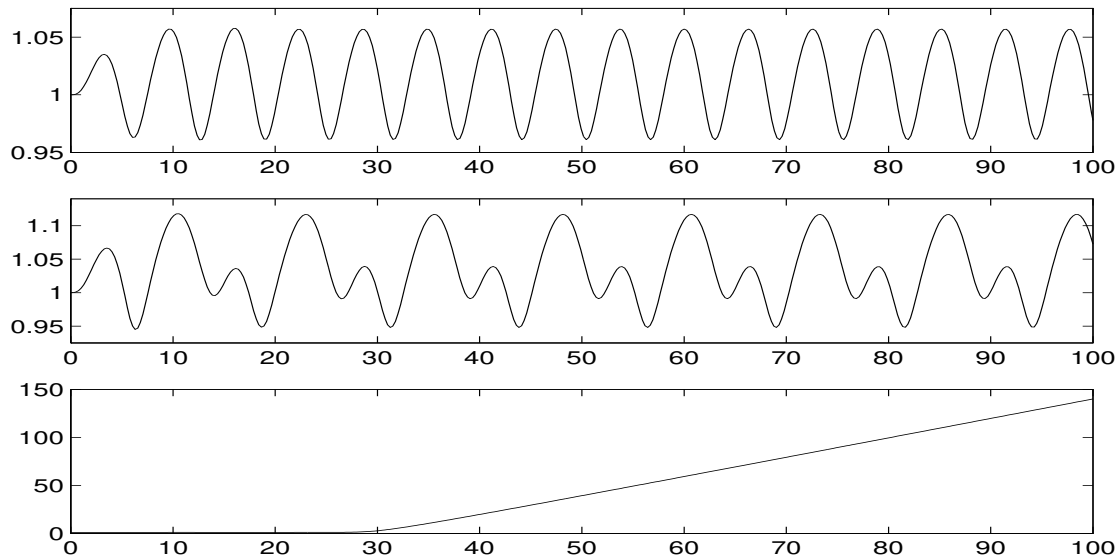
PF#1091, Harkin, Nadim and Kaper – Figure 8



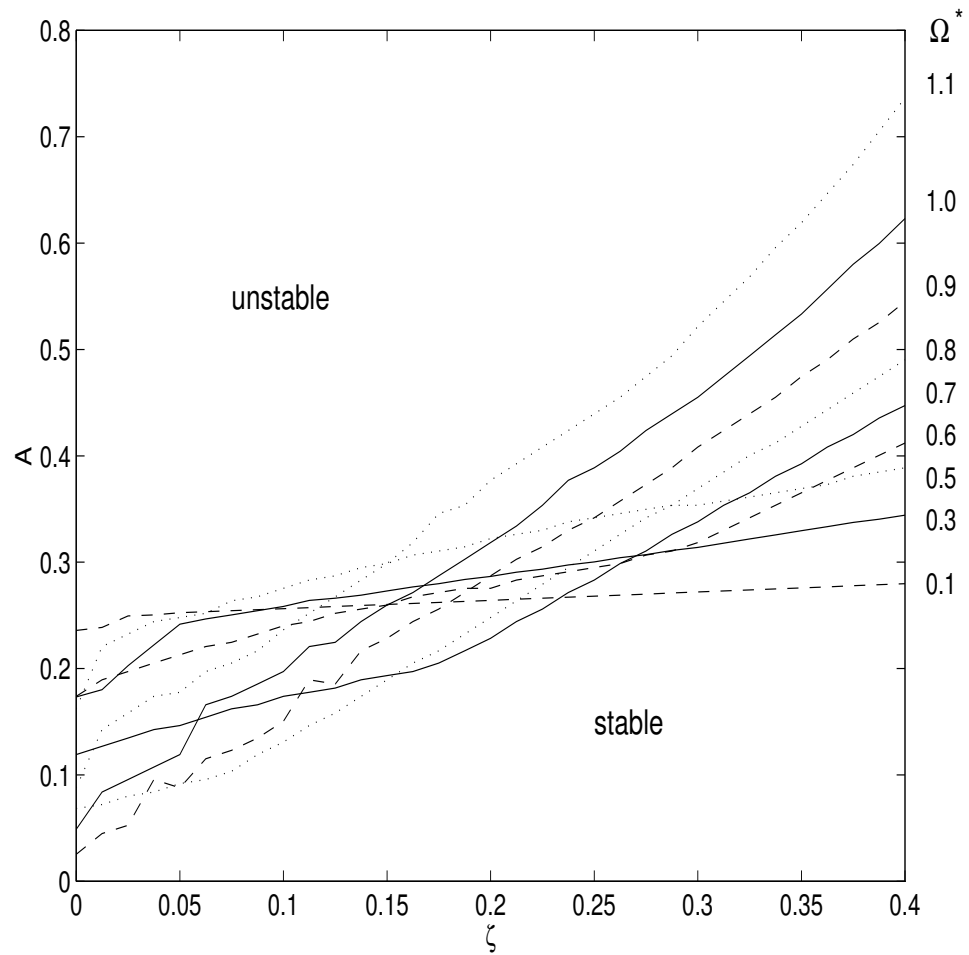
PF#1091, Harkin, Nadim and Kaper – Figure 9



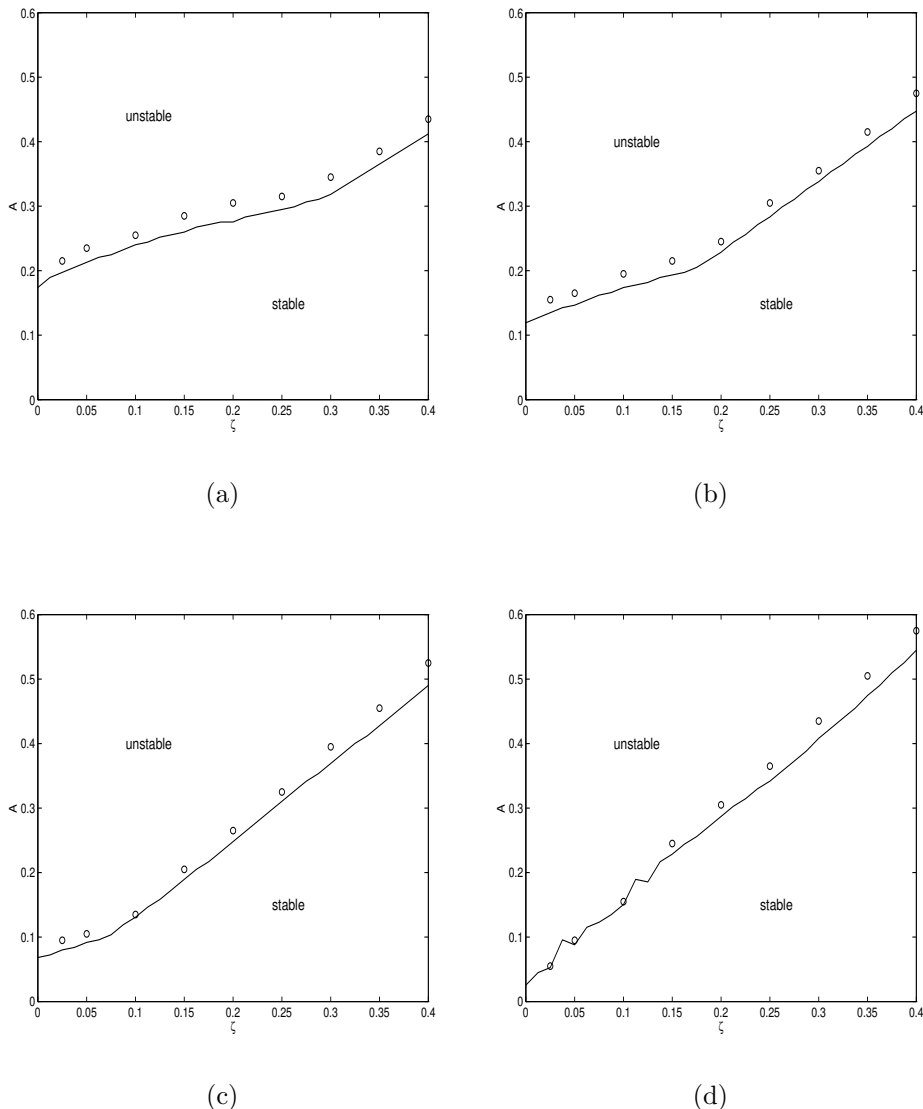
PF#1091, Harkin, Nadim and Kaper – Figure 10



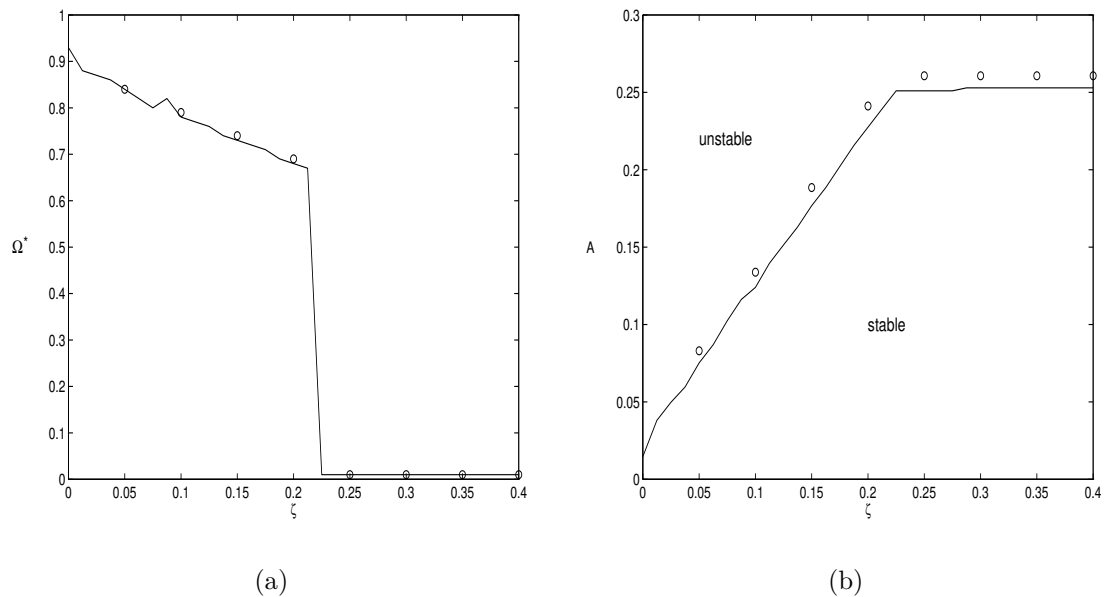
PF#1091, Harkin, Nadim and Kaper – Figure 11



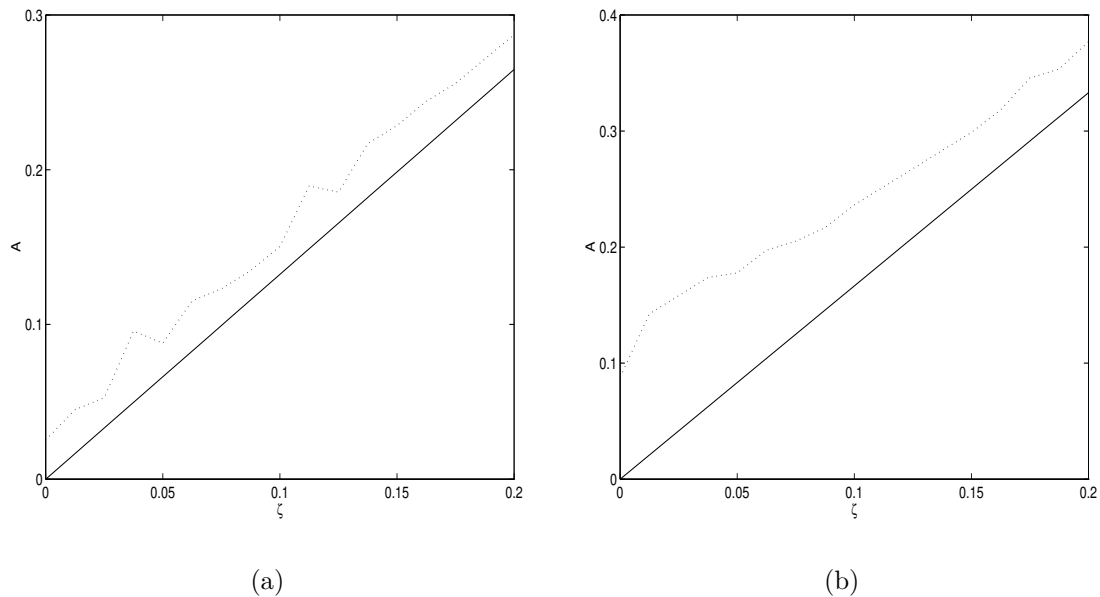
PF#1091, Harkin, Nadim and Kaper – Figure 12



PF#1091, Harkin, Nadim and Kaper – Figure 13



PF#1091, Harkin, Nadim and Kaper – Figure 14



PF#1091, Harkin, Nadim and Kaper – Figure 15

